IEEE Access
Multidisciplinary | Rapid Review | Open Access Journal

Received April 26, 2019, accepted May 17, 2019, date of publication June 5, 2019, date of current version June 21, 2019.

Digital Object Identifier 10.1109/ACCESS.2019.2920890

Frequency Characteristics of Geometry-Based Clusters in Indoor Hall Environment at SHF Bands

PANAWIT HANPINITSAK[1], (Student Member, IEEE), KENTARO SAITO[1], (Member, IEEE), WEI FAN[2], (Senior Member, IEEE), JOHANNES HEJSELBÆK[3], (Member, IEEE), JUN-ICHI TAKADA[1], (Senior Member, IEEE), AND GERT FRØLUND PEDERSEN[2], (Senior Member, IEEE)

[1]Department of Transdisciplinary Science and Engineering, Tokyo Institute of Technology, Tokyo 152-8552, Japan
[2]Department of Electronic Systems, Aalborg University, DK-9220 Aalborg, Denmark
[3]Nokia Bell Labs, DK-9220 Aalborg, Denmark

Corresponding author: Panawit Hanpinitsak (hanpinitsak.p@ap.ide.titech.ac.jp)

This work was supported by the Japan Society for the Promotion of Science (JSPS) KAKENHI under Grant 16K18102 and Grant 19K04369.

ABSTRACT This paper presents an analysis of geometry-based cluster frequency dependency at super-high-frequency bands, including 3, 10, and 28 GHz. First, multipath components were extracted from the measured data by using the space-alternating generalized expectation-maximization algorithm. Then, geometry-based clusters were estimated by using the enhanced scattering point-based KPowerMeans (SPKPM) algorithm. Finally, the frequency dependencies of their scattering intensities were discussed with the assistance of physical optics. The analysis results showed that the SPKPM could also be applied to obtain reasonable scattering locations at multiple frequencies in most cases. In addition, reflection on smooth surfaces was the dominant mechanism of clustering where there was no frequency dependence, whereas diffraction, scattering, and shadowing were significant causes of frequency dependence. Assuming that the line-of-sight is obstructed, diffraction, scattering, and shadowing accounted for 30–40% of the entire channel in terms of power, which was not negligible and thus the channel was largely frequency-dependent. The analysis results are expected to provide crucial insights for multiple-frequency channel modeling for fifth-generation wireless systems.

INDEX TERMS Radio propagation, SHF bands, indoor, MPC clustering, channel models, physical optics.

I. INTRODUCTION

Owing to the large available bandwidth and the possibility to construct a compact antenna array with a large number of elements, millimeter wave (mmWave) bands have been suggested as the primary enabler of fifth-generation (5G) communication systems [1], [2], in order to accommodate a dramatic increase in data traffic. However, the transmitted signals suffer from larger free space path loss in these bands. Furthermore, the performance is more susceptible to shadowing and mobile station movement. Thus, to compensate for these effects as well as to ensure compliance with strict regulations, it is possible that a very large bandwidth or several subbands from the microwave to mmWave bands may be exploited for 5G systems, and the target frequency to be used for 5G, as discussed at the World Radiocommunication Conference (WRC)-15, varies considerably [3]. Therefore, it is important to fully understand the frequency dependency of the channels in wide frequency ranges to facilitate multiple-frequency channel model creation [4].

Because of its significance, there have recently been studies considering the channel frequency dependency at various ultrahigh frequency (UHF), superhigh frequency (SHF), and extremely high frequency (EHF) bands in indoor environments. Aalborg University compared the power-angular-delay profile (PADP) and validated with ray tracing at 3, 15, and 29 GHz [5], [6]. They also proposed a new ultrawideband (UWB) channel sounding system and compared the PADP and impulse responses (IRs) at 19, 26, 29, and 39 GHz [7]. In [8], researchers from Ericsson compared the

The associate editor coordinating the review of this manuscript and approving it for publication was Jose Saldana.

PADP using a cubic array at the 5.8, 14.8, and 58.7 GHz bands [8]. A New York University research group studied path loss (PL) and delay spread (DS) characteristics at 28 and 73 GHz [9], [10] in an office scenario. Aalto University compared the power delay profile (PDP), angular power spectrum (APS), path angle distribution, DS, specular power, and diffuse component power between 60 and 70 GHz and provided a ray-based channel model in an office, train station, and mall [11], [12]. They also compared similar parameters in an airport terminal [13] at the 2, 15, 28, and 60 GHz bands. In addition, they conducted a comparison of the APS and path angle distribution between 4, 15, and 28 GHz in an office environment [14]. [15] analyzed the DS, PL, and frequency selectivity between 5 and 60 GHz in a meeting room. Sasaki *et al.* [16] proposed a PL model as a function of frequency from 0.8 to 37 GHz. Huang *et al.* provided a comprehensive comparison between the 11, 16, 28, and 38 GHz bands and presented some preliminary cluster birth–death properties [17]. [18] derived PL and DS characteristics at 3.5, 6, 14, 23, 26, and 28 GHz [18]. [19] compared large-scale parameters (LSP) from 2 to 22 GHz, including the PL, shadow fading (SF), PDP, DS, and capacity. In [20], [21], LSPs and parameter-based cluster parameters between 28 and 38 GHz were compared. Reference [22] compared PL, parameter-based cluster dispersion, DS, and angular spread (AS) at 62 and 83.5 GHz. The authors also compared the PL and PADP in a classroom from 3 to 28 GHz [23] and AS and DS characteristics from 10 to 28 GHz in a large hall [24].

As wireless performance strongly relies on the propagation environment, channel characterization is needed for the optimization and planning of wireless links. It is also observed that multipath components (MPCs) in the environment arrive as clusters [25], [26], where each cluster consists of MPCs with similar trajectories. Conventionally, clusters are grouped based on the propagation parameters' closeness [27]. This is called parameter-based clustering. Moreover, they are all randomly generated in angle and delay domains in stochastic models, such as the 3GPP fast fading model [28] for the system evaluation. As frequency dependency analyses are needed, the statistical properties of parameter-based clusters, such as AS and DS, among different frequencies were also compared in [20]–[22].

As the measurements from these studies were conducted in various types of environments with different interacting objects (IOs), the frequency dependency of clusters' statistical properties and the results of stochastic models may become inconsistent [29]. This is because the channel property depends on the physical propagation mechanism behind each IO in the environment. Each IO could also be interpreted as a cluster of specular and diffuse MPCs [26]. This is called geometry-based clustering [30], [31]. As these inconsistencies lead to an unclear conclusion about the channel frequency dependency, the clarification and understanding of the physical mechanism of each geometry-based cluster or IO at several frequency bands are essential insights to improve the model. However, most of the cluster physical interpretation studies only focus on a single frequency band, such as indoor 11 GHz [30] or an outdoor suburban scenario at 300 MHz [31]. To the best knowledge of the authors, geometry-based cluster comparisons of the UHF and SHF bands, as well as their interpretations based on electromagnetic simulations have not been reported in the open literature. By conducting a geometry-based cluster physical interpretation of frequency dependency, we can gain more insight into the physical mechanisms of the inconsistencies.

In light of these issues, this paper presents the frequency dependency of geometry-based clusters at the UHF and SHF bands. As a preliminary step, the space-alternating generalized expectation-maximization algorithm (SAGE) was used to estimate the angle-of-arrival (AoA), elevation of arrival (EoA), and delay time (DT) of the MPC parameters from measurement data [32]. Our contributions and enhancements in relation to our previous papers [23], [24] are divided into three aspects: First, we identified the geometry-based clusters and IOs in the propagation environment automatically by applying the scattering point-based KPowerMeans (SPKPM) algorithm to the SIMO channel to estimate the geometry-based clusters. SPKPM was already proposed by the authors in [30], [33], but only applied to the 11 GHz channel. This approach is also different from that of [31], which utilizes visual inspection to obtain the geometry-based clusters. Second, we clarified the factors that caused the cluster frequency dependency utilizing physical optics (PO) [34] simulations. Finally, we quantitatively evaluated the cluster frequency characteristics using scattering intensities (SI) [35]. The clusters were also categorized into different groups based on the mechanism and the power percentage of each group was computed to clarify its importance. Therefore, the results are expected to be utilized for the channel modeling and model parameter determination for 5G systems. The results showed that the power percentage of specular reflection clusters were dominant in this environment. The frequency dependency of specular reflection was not significant, because the reflection coefficients in these bands are not so different [36], [37]. However, the clusters that were classified into shadowing, scattering, diffraction, and the Fresnel zone plate effect had significant frequency dependencies.

The remainder of this paper is organized as follows: In Section II, the measurement-based data analysis is briefly described. Section III briefly explains the PO algorithm and demonstrates its applicability in a simple scattering scenario. Section IV explains the channel measurement and data analysis parameters used. In Section V, the frequency dependency and physical interpretation of geometry-based clusters are discussed. Finally, the paper is summarized in Section VI.

LIST OF ACRONYMS

AoA	Angle-of-Arrival
AS	Angular Spread
DB	Double Bounce

DBSP	Double Bounce Scattering Point
DS	Delay Spread
DT	Delay Time
EoA	Elevation-of-Arrival
IO	Interacting Object
KPM	KPowerMeans
LOS	Line-Of-Sight
MBRT	Measurement-Based Ray Tracer
MCD	Multipath Component Distance
MIMO	Multiple-Input Multiple-Output
MPCs	Multipath Components
OLOS	Obstructed Line-Of-Sight
PDP	Power-Delay-Profile
PEC	Perfect Electric Conductor
PL	Path Loss
PO	Physical Optics
SAGE	Space-Alternating Generalized Expectation-Maximization
SB	Single Bounce
SBSP	Single Bounce Scattering Point
SI	Scattering Intensity
SIMO	Single-Input Multiple-Output
SP	Scattering Point
SPP	Stationary Phase Point
SPD	Scattering Point Distance
SPKPM	Scattering Point-Based KPowerMeans
TB	Triple Bounce
TBSP	Triple Bounce Scattering Point

II. MEASUREMENT-BASED DATA ANALYSIS

The data analysis can be divided into two parts, as depicted in Fig. 1: 1. Measurement-based and 2. Theory-based using PO [34]. In the measurement-based analysis, MPC parameters and scattering points (SPs) were estimated from the channel sounder [5], [6] using SAGE [32] and an enhanced measurement-based ray tracer (MBRT) [30], [33]. These SPs can be divided into single bounce (SB) SPs (SBSPs), double bounce (DB) SPs (DBSPs), and triple bounce (TB) SPs (TBSPs). Next, geometry-based clusters were estimated using (SPKPM) [30]. For compactness, geometry-based clusters will hereinafter be referred to as clusters. The clusters were then recombined to account for the inaccuracies and ambiguities of higher-order bounce cluster estimation. Lastly, they were tracked using the multipath component distance metric (MCD) [38]. Because MBRT may have the ambiguity of the SP estimation, the PO simulation [34] with a large calculation area was utilized for the detailed identification of propagation characteristics and to compensate for this ambiguity. In PO [34], object models were created by dividing the surface into small triangular meshes characterized by a normal vector and vertices [39]. For each mesh, the surface currents and vector potentials were computed. Finally, the mesh electric fields were computed. The phase of each mesh was utilized as a tool to interpret the frequency characteristics of the clusters. It should be noted that these implementations were independently applied to the channels at each frequency.

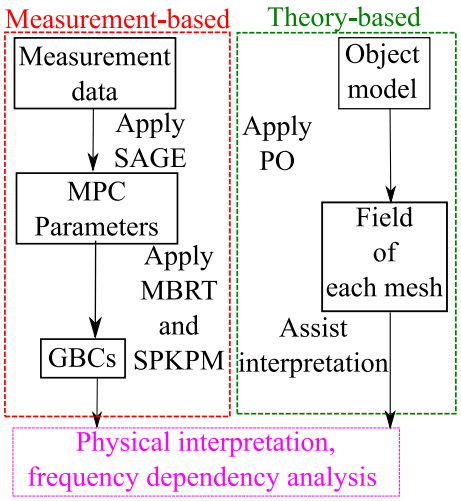

FIGURE 1. Flow chart of data analysis method.

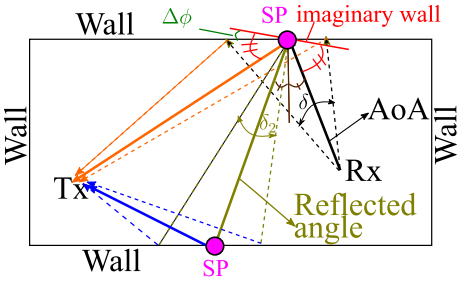

FIGURE 2. Demonstration of SIMO MBRT concept.

A. SIMO-BASED MEASUREMENT-BASED RAY TRACER

MBRT [40] is a tool to estimate the SP of each MPC, which is obtained from the parameter estimation, by utilizing a geometric map of the environment. In [30], it was modified to be used with MIMO measurement data by launching the rays from both the Tx and Rx sides. Because the measurement in this study utilized a single-input, multiple-output (SIMO) system, the algorithm was modified to be applicable to the present system by launching the rays only from the Rx side. Both the AoA and DT were utilized to minimize the ambiguity of higher-order bounce SP estimation. In the preprocessing step, the LOS cluster is removed. The LOS cluster is the group of MPCs around the LOS region, which is simply calculated from the Tx and Rx positions. After that, the SB, DB, and TB MBRT algorithms are executed.

Fig. 2 briefly illustrates the concept of MBRT. Similar to the approach in [30], for each MPC, several rays are launched from the Rx with an angular range of $\pm\delta/2$ with respect to the AoA obtained from SAGE, and their intersection points with the wall are computed to find the SPs. If the algorithm is SB, in the second step, the lines that pass through those intersection points and the Tx are calculated (orange lines), and the delay error ($\Delta\tau$) and reflection angle error ($\Delta\phi$) are computed. The delay error is defined as the difference between delay obtained from SAGE and delay obtained from

the SP location, whereas the reflection angle error is defined as the angle difference between the actual wall and the imaginary wall, where the incident angle is equal to the reflected angle, as shown in Fig. 2. Finally, the rays where $\Delta\tau > \epsilon_{\tau,\mathrm{SB}}$ or $\Delta\phi > \epsilon_{\phi,\mathrm{SB}}$ are discarded. $\epsilon_{\tau,\mathrm{SB}}$ and $\epsilon_{\phi,\mathrm{SB}}$ are the SB delay and angle thresholds, respectively. If the algorithm is DB or TB, the reflected angle from each SP is calculated based on the specular reflection assumption. Then, several rays with the angular range of $\pm\delta_2/2$ with respect to this reflected angle are launched, and the intersection points with the wall are calculated to find the SPs of the second interaction from the Rx (dark yellow lines). If the algorithm is TB, the aforementioned steps are repeated to find the SPs of the third interaction from the Rx. Next, the lines that pass through those intersection points and Tx are computed (blue lines). Finally, the rays where $\Delta\tau > \epsilon_{\tau,\mathrm{DB/TB}}$ or $\Delta\phi > \epsilon_{\phi,\mathrm{DB/TB}}$ are discarded. $\epsilon_{\tau,\mathrm{DB/TB}}$ are the DB and TB delay thresholds, and $\epsilon_{\phi,\mathrm{DB/TB}}$ are the DB and TB delay thresholds.

After all the candidate SB, DB, and TB SPs are computed for each MPC, the one which has the minimum $\Delta\tau$ among them is selected as the representative SP of the respective MPC.

B. SCATTERING POINT-BASED KPOWERMEANS ALGORITHM

After obtaining all types of SPs, they are clustered separately utilizing SPKPM [30]. The concept of SPKPM is to group MPCs based on minimizing the physical distance between SPs of the same cluster, which is the SP distance (SPD). Thus, the algorithm can be expressed by minimizing the parameter $D_{\mathrm{SB/DB/TB}}$.

$$D_{\mathrm{SB/DB/TB}} = \sum_{l=1}^{L_{\mathrm{SB/DB/TB}}} P_l \cdot \mathrm{SPD}(x_{l,\mathrm{SB/DB/TB}}, c_{I_l,\mathrm{SB/DB/TB}}) \tag{1}$$

where $L_{\mathrm{SB/DB/TB}}$ is the number of MPCs in each category, and P_l and $x_{l,\mathrm{SB/DB/TB}}$ are the power and parameter vector of path l, respectively. $c_{I_l,\mathrm{SB/DB/TB}}$ is the cluster centroid to which path l belongs. The SPD between two MPCs is defined as the Euclidean distance between two parameter vectors. For the SB case, the parameter vector is the vector of the x- and y- coordinates of a single SP from a single IO. For the DB case, it is the vector of the Cartesian coordinates of two SPs from two IOs. Similarly, the vector of x- and y- coordinates of three SPs from three IOs represents the parameter vector of TB clusters. The remaining procedures of SPKPM are provided in detail in [30].

C. CLUSTER RECOMBINATION AND TRACKING

Because only angular information on the Rx side is known for SIMO, and the measurement resolution is limited, the misjudgments of the SP and cluster estimations are inevitable, especially for DB and TB clusters. To mitigate this problem, after obtaining all the clusters, they are coarsened by combining clusters that have similar DT and AoA centroids. In the first step, the MCDs between all pairs of clusters are calculated. Then, the pair that yields the minimum MCD is combined into one cluster. These processes are repeated until the AoA and DT centroid differences between any two arbitrary clusters are larger than the thresholds δ_c and $\Delta\tau_c$, respectively.

In the final step, the combined clusters are tracked by comparing the MCDs between the current and previous snapshots. If the cluster is not found in the previous snapshot, the latest snapshot where this cluster is found is used instead.

D. CLUSTER MATCHING AMONG DIFFERENT FREQUENCIES

After all the clusters are calculated and tracked for each frequency, the matching of the same clusters at different frequencies is performed through visual inspection by checking the tracked clusters from both 1. the cluster centroid tracking results in the AoA–DT domain and 2. the geometric map. These two criteria were used because the AoA and DT centroids of the same clusters at different frequencies should be similar. Moreover, the same clusters at different frequencies should come from the same major IO or IOs in the environment. It was found that AoA and DT centroids of the same clusters at different frequencies were very similar. Moreover, in case of SB clusters, the IOs matched well among different frequencies. Nevertheless, owing to the ambiguity of the DB and TB cluster estimation, the IOs of these clusters were not exactly matched among different frequencies at a few snapshots. However, these mismatches were negligible, as most of these clusters were combined with the SB clusters, which had much higher power. The IOs of the SB clusters also matched well.

E. SI CALCULATION

The cluster SI is calculated from the cluster power and delay centroid. First, the reconstructed band-limited channel transfer function $H_k(f)$ and IR $h_k(\tau)$ based on a single isotropic antenna for the k-th cluster, and its delay centroid can be expressed by

$$H_k(f) = \sum_{p\in\mathcal{C}_k} \gamma_p \exp\left(-j2\pi f \tau_p\right) \tag{2}$$

$$h_k(\tau) = \sum_{n=0}^{N-1} H_k(f_n) \exp\left(j2\pi f_n \tau\right) \tag{3}$$

$$\bar{\tau}_k = \frac{\sum_{p\in\mathcal{C}_k} |\gamma_p|^2 \cdot \tau_p}{\sum_{p\in\mathcal{C}_k} |\gamma_p|^2} \tag{4}$$

where τ_p and γ_p are the delay and path weight of the p-th MPC. $\mathcal{C}_k$ is the set of MPC indices in cluster k. n, N, and $\bar{\tau}_k$ are the frequency index, total number of frequency points, and delay centroid of cluster k, respectively.

Then, the power and SI of cluster k are calculated based on the summation of the power of every IR delay bin:

$$P_k = 10\log_{10}\left(\sum_{\tau}|h_k(\tau)|^2\right) \quad (5)$$

$$SI_k = P_k - 20\log_{10}\left(\frac{\lambda}{4\pi c\bar{\tau}_k}\right) \quad (6)$$

where λ and c are wavelength and speed of light.

III. SIMULATION-BASED ANALYSIS

A. PHYSICAL OPTICS ALGORITHM

The PO algorithm [34] is implemented in three cases: 1. SB PO, 2. DB PO, and 3. SB PO with shadowing.

First, the source, observation, and object positions are initialized, where the object is divided into several triangular meshes. Then, the illuminating meshes are determined based on the orientation of their normal vectors with respect to the source and observation positions [41]. Next, the incident electric and magnetic fields on the illuminating meshes are computed based on the point source assumption, in which the direction of the fields change with the mesh positions. In the next step, the surface currents are calculated based on the reflection coefficient, incident fields, and normal vector directions of each mesh. The reflection coefficients are calculated independently for each polarization by using the Fresnel coefficients [42]. In the case of multiple-layer objects, the total reflection coefficient is calculated using the transmission line equations [42]. After that, the vector potentials are computed by the surface integration of the surface currents using the Ludwig integration algorithm [43], [44]. The electric and magnetic fields of each mesh are then calculated from the vector potentials. Thus, in the case of a perfect electric conductor (PEC), the scattered electric field at mesh m ($E_{s,m}$) can be computed by

$$E_{s,m} = W_m \cdot \left(j\omega\mu\frac{\hat{\boldsymbol{n}}_m \times \boldsymbol{H}_{i,m}\lambda}{8\pi^2} I_m \times \hat{\boldsymbol{r}}_{s,m} \times \hat{\boldsymbol{r}}_{s,m}\right) \quad (7)$$

where $\hat{\boldsymbol{n}}_m$, $\boldsymbol{H}_{i,m}$, and $\hat{\boldsymbol{r}}_{s,m}$ are the normal vector, incident magnetic field, and unit scattered vector at mesh m, respectively. W_m is the windowing function, which will be discussed later. I_m is the integrand of mesh m, which can be expressed by the surface integral over the mesh area:

$$I_m = \int_S \frac{e^{-j(k_{s,m}(o-q_m)+k_{i,m}(q_m-s))}}{|q_m-s||o-q_m|}\mathrm{d}S \quad (8)$$

where $\boldsymbol{k}_{s,m}$, $\boldsymbol{k}_{i,m}$, and $\boldsymbol{q}_m$ are the scattered and incident wavenumber vectors and the mesh position vector at mesh m, respectively. $\boldsymbol{o}$ and $\boldsymbol{s}$ are the observation and source position vectors. From eq. 8, it can be observed that the phase of the integrand changes according to the path length from the source and observer to the mesh. The area where the phase changes very rapidly has almost zero contribution, owing to the cancellation effect. Thus, the integral over the whole area can be approximated by the contribution from the stationary phase point (SPP), where the phase changes slowly and can be interpreted as a specular reflection area, and the edges of the object, which can be interpreted as diffraction points [45]. Therefore, if the SPP area is present, which dominates the diffraction effect, the integral area is truncated by using the window function based on the Fresnel zone difference (denoted by W_m in eq. 8) between an arbitrary mesh and a specular reflection point using the third zone boundary ($\Delta n_B = 3$) [45]. Otherwise, the whole object is integrated to include the diffraction effect.

In case of SB PO, after the fields at each mesh are calculated, the total fields at the observation point are computed from the summation of all the mesh fields. On the contrary, for DB PO, the total incident fields on the second IO are computed by the summation of all the mesh fields from the first IO. The computation time is reduced by computing the fields on coarser meshes (0.2λ) first and then interpolating into the fine meshes (0.1λ) using the nearest neighbor interpolation method. After that, the surface currents and vector potentials of the second IO are computed by using the Ludwig algorithm [43], [44], and the total fields at the observation are computed from the summation of all the mesh fields.

There are four steps in the SB PO with shadowing calculation. First, the SB PO algorithm is executed on the scattering object to obtain the total field without shadowing. Second, imaginary meshes with free-space wave impedance are created on the shadowing object as a plane and also using the window function [45]. Third, the DB PO algorithm is performed on the scattering and shadowing objects to obtain the total shadowed field. Finally, the total nonshadowed field is computed by subtracting the shadowed field from the field without shadowing.

B. PO DEMONSTRATION USING PEC PLATE

To verify the applicability of the implemented PO algorithm, it was applied to a simplified scattering scenario. Fig. 3 (a) shows the configuration of the validation with Cartesian coordinates, where a 2 m × 2 m PEC plate was fixed on the x-axis. The Tx and Rx were placed at the same position, which was 3 m from the plate in the y-direction, and they were moved along the x-direction at different distances d. d was set to zero where the normal projections of the Tx and Rx onto the x-axis were on the left edge of the plate. d increased as the Tx and Rx moved to the left, and decreased as they moved to the right. In other words, the normal projections of the Tx and Rx onto the x-axis were inside and outside the plate when d was negative and positive, respectively. Fig. 3 (b) illustrates SI at different d for three different frequencies: 3, 10, and 28 GHz. Fig. 3 (c) depicts the phase plot of the integrand from eq. 8 at each mesh position on the plate. The black circular lines indicate the Fresnel zone rings, which were calculated in relation to the specular reflection distance. As shown in Fig. 3 (b), the characteristics could be divided into five zones. When all three Fresnel zones were on the plate, SI became zero owing to the specular reflection, as shown in the first zone. When the constructive interference from the third Fresnel zone disappeared at the edge of the

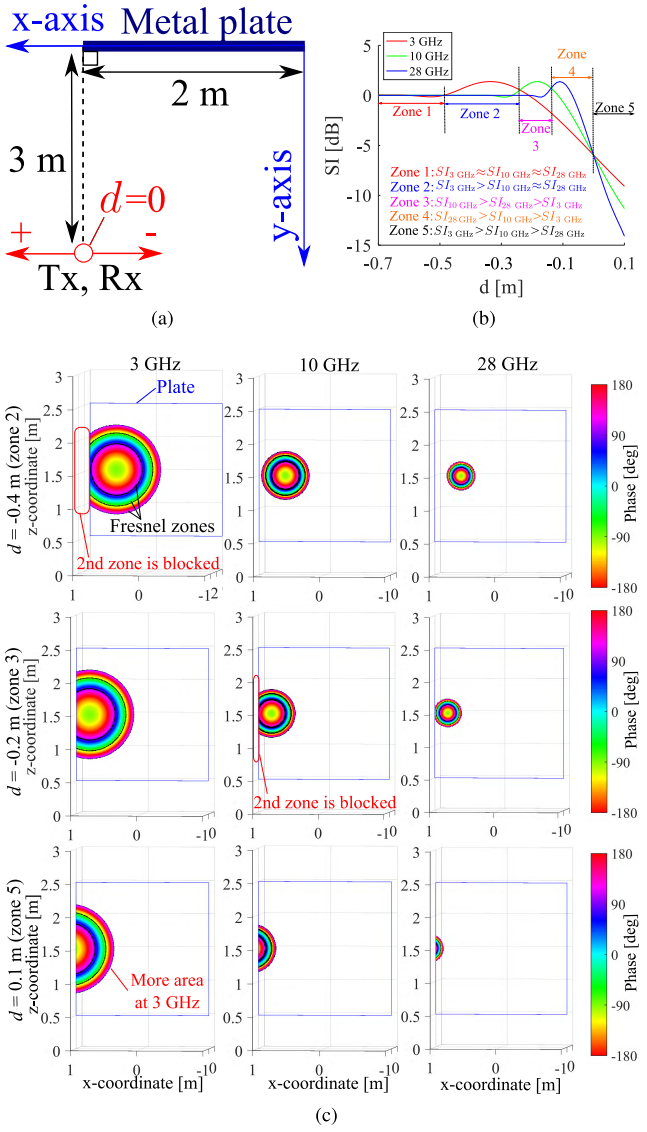

FIGURE 3. Scattering validation illustration ((a) Configuration, (b) Distance and SI plot, (c) Phase of mesh plot).

plate, SI became slightly smaller than zero. In the second zone, the SI of 3 GHz was above zero and larger than the other two frequencies. This was because the destructive interference from the second zone vanished at the edge. Thus, only the constructive phase of the first zone remained, and the total SI was larger than zero. This phenomenon is similar to the Fresnel zone plate effect [46]. This type of mechanism is also observed in knife edge diffraction theory [47]. Because the Fresnel zone of 3 GHz was the largest, this effect occurred at smaller d than other frequencies. As d increased, the first Fresnel zone of 3 GHz started to disappear, the Fresnel zone plate phenomenon started to appear at 10 GHz, and SI at that band became the largest, as shown in zone 3. In zone 4, the normal projections of the Tx and Rx onto the x-axis were still inside the plate but almost at its edge, and thus the Fresnel zone plate occurred at 28 GHz, which made the SI at 28 GHz become the largest. Because $d = 0$ was

TABLE 1. Channel sounder specification.

Parameters	Values
Center frequency	3, 10, 28 GHz
Bandwidth	2 GHz
Tx antenna	Commercial biconical antenna (A-INFO SZ-2003000)
Rx antenna	Modified biconical antenna [48]
Number of Rx elements	360
UCA radius	0.24 m
Number of frequency bins	750
Maximum delay	375 ns
Tx and Rx height	1.5 m

FIGURE 4. Photograph of Tx and Rx.

when the normal projections of the Tx and Rx onto the x-axis were at the left edge of the plate, exactly half of the Fresnel zone was scattered, creating a 6-dB loss and the same SI for all three frequencies. Finally, if d became positive, the edge diffraction effect became prominent and the SI at lower frequencies was larger than that at higher frequencies, owing to the larger Fresnel zones at that band. These results imply that the scattering effects at different positions create strong frequency characteristics due to the difference in the Fresnel zone sizes, which will be discussed in Section V.

IV. SHF BAND CHANNEL MEASUREMENT AND PO OBJECT MODEL

The channel sounding campaign was performed by using a vector network analyzer (VNA)-based virtual uniform circular array (UCA) system [5], [7]. The specifications of the channel sounder are shown in Table 1. The center frequencies were 3, 10, and 28 GHz. The bandwidth was set to 2 GHz and was fixed for all three bands to ensure a fair comparison of the frequency characteristics. Fig. 4 shows a photograph of the Tx and Rx antennas. The Tx was a single commercial biconical antenna, and the Rx was a modified biconical antenna [48] mounted on a robot arm, which rotates in a circular motion to mimic the UCA system. Fig. 5 shows the block diagram of the sounding system, which consists of five main parts: 1. vector network analyzer (VNA), 2. local oscillator (LO)/intermediate frequency (IF) distribution unit to divide the LO signal to mixers, 3. test and 4. reference mixers to down-convert the received and transmitted signals to an IF signal, and 5. automatic rotator to rotate the antenna

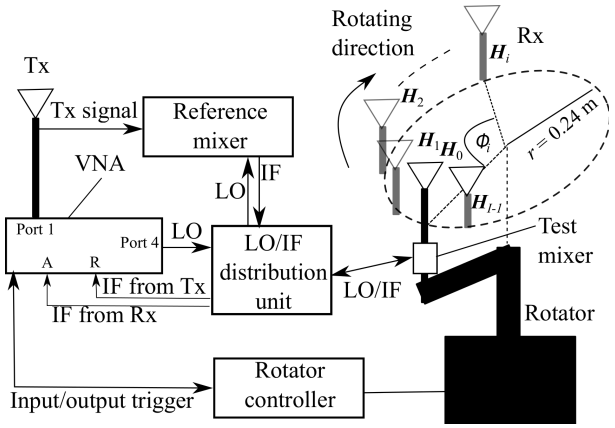

FIGURE 5. Virtual UCA system.

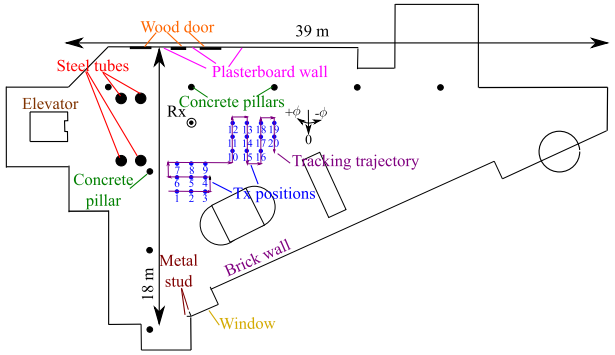

FIGURE 6. Measurement floor plan in hall environment.

after each measurement sweep. The measurements were conducted in a hall environment [49], which is a large room with few scattering objects. The floor plan as well as 20 Tx snapshots and major objects along with their corresponding PO models are depicted in Fig. 6 and 7. The Tx numbering and arrows in Fig. 6 represents the tracking trajectory. The elevator, tubes, and stud are homogeneous and made from steel. The pillars are made from concrete. The depth from the surface of the brick to the mortar is 2 mm for the brick wall. The plasterboard wall is built by mounting plasterboard sheets on top of PEC stud and mineral wool [50]. The wood door is a laminate Formica wood with solid wool in between [51], which is supported by a steel frame. The window is made from glass covered with a thin metallic layer.

In the data analysis, propagation parameters were estimated by using the SAGE algorithm [32], [52] with a spherical wave model [53], [54]. Although the frequencies at the 3 GHz band change significantly from 2 to 4 GHz, the algorithm was able to detect the strong reflection paths, and the spurious paths were not detected. Thus, more than 80% of the channel power could be extracted by the algorithm. Clusters were then extracted from those MPCs using SPKPM [30]. Table 2 provides the parameters used to estimate the clusters. The value in the right column is taken as 3 GHz / 10 GHz / 28 GHz if there are three values. If the values of all the frequencies are the same, only a single

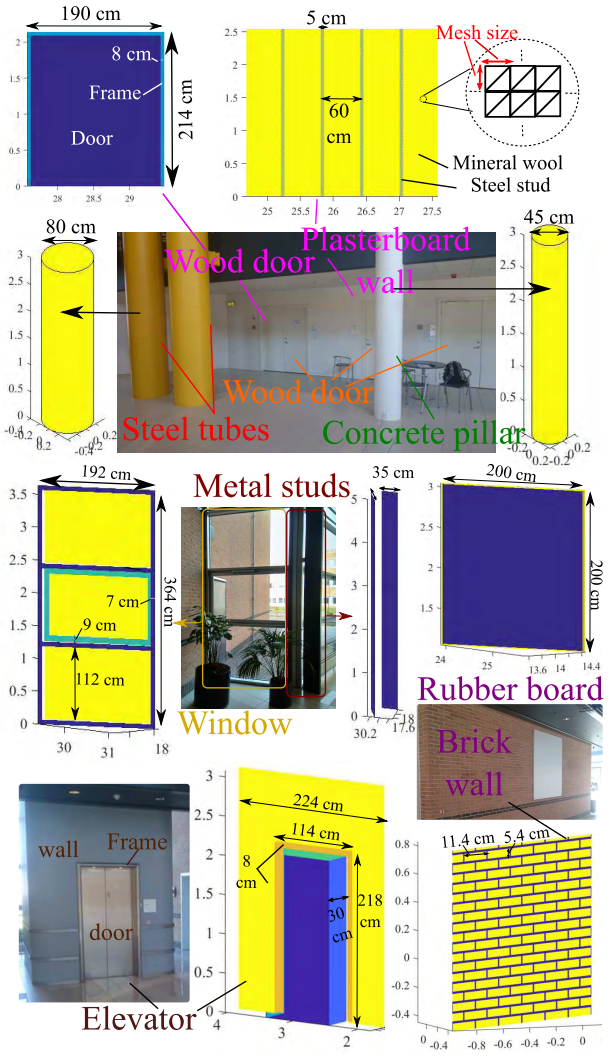

FIGURE 7. Major objects and their corresponding models.

number is shown. These parameters were obtained based on a heuristic approach, which is largely dependent on many factors such as the room size and distance between the IO and Tx/Rx. The guidelines on how to choose these parameters are explained in [30]. For non-PEC materials, the conductivity was assumed to be zero. Thus, each material's relative permittivity was the same across all three bands, which were obtained through tuning the received power PO results with the measurement. For PEC materials, i.e., elevator, stud, and tube, the conductivity was assumed to be infinite for all three bands.

V. RESULTS AND DISCUSSION

A. RAY TRACING, CLUSTERING, AND TRACKING RESULTS

Fig. 8 depicts the SB, DB, and TB clustering results of SPs and a scatter plot of the clusters in the first snapshot. Circles represent SPs, which are color-coded based on the clustering results. SPs of the same color belong to the same cluster. In the scatter plot, the SB, DB, and TB MPCs are denoted by circles, upward pointed triangles, and right pointed triangles,

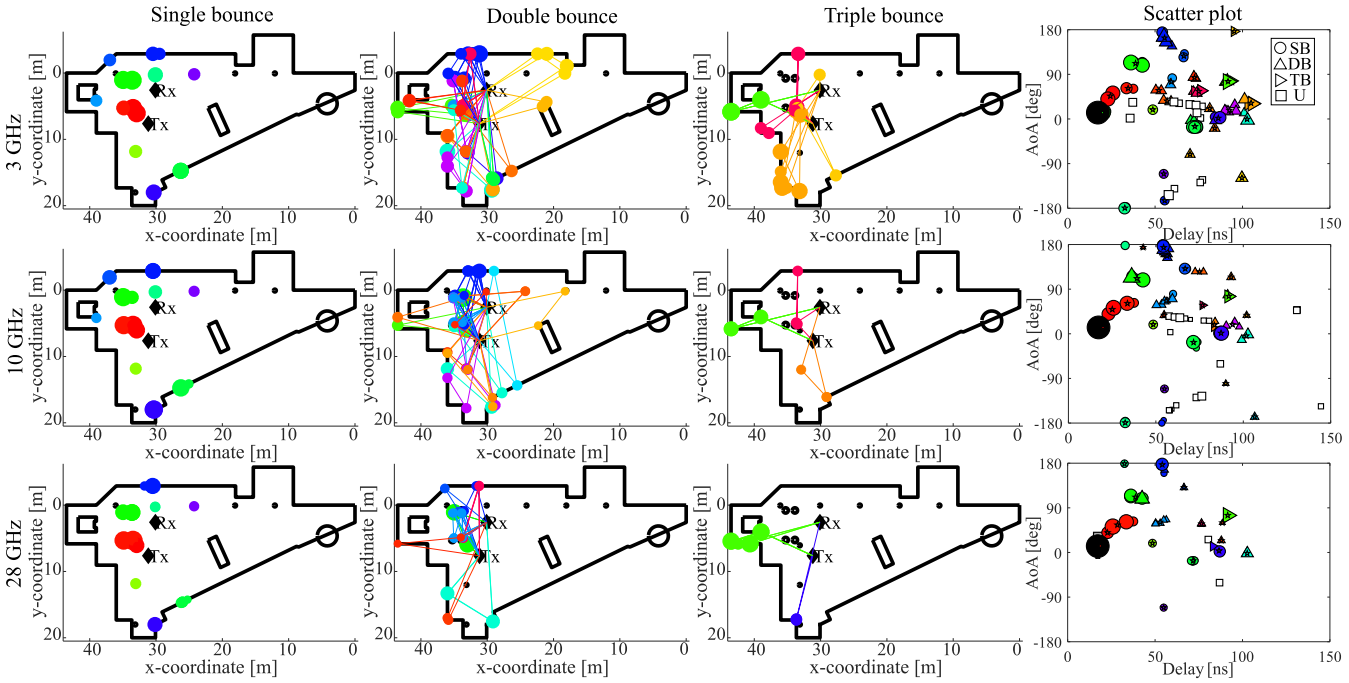

FIGURE 8. SB, DB, and TB MBRT and clustering results of the first snapshot.

TABLE 2. Parameters used in the analysis.

Parameters	Value
SAGE algorithm	
Number of MPCs	100
Iteration number	43
MBRT	
δ	14°
δ_2	20°
$\epsilon_{\tau,\mathrm{SB}}$, $\epsilon_{\tau,\mathrm{DB}}$, $\epsilon_{\tau,\mathrm{TB}}$	5 ns
$\epsilon_{\phi,\mathrm{SB}}$, $\epsilon_{\phi,\mathrm{DB}}$, $\epsilon_{\phi,\mathrm{TB}}$	10°
SPKPM parameters, cluster recombining parameters	
$K_{\min}$ (SB)	2
$K_{\max}$ (SB)	25/20/15
$K_{\min}$ (DB)	5/2/2
$K_{\max}$ (DB)	25/15/10
$K_{\min}$ (TB)	2
$K_{\max}$ (TB)	10
Maximum iteration	100
$\Delta\tau_c$	8 ns
δ_c	15°
Physical optics parameters	
Mesh size	0.1λ
DB coarse mesh size	0.2λ
Relative permittivity (ϵ_r)	PEC (elevator, stud, tube), 7 (wood), 10 (brick) 3.5 (plasterboard), 1.5 (rubber), 9.5 (solid wool) 5.8 (concrete), 14 (mortar), 6 (mineral wool)
Relative permeability (μ_r)	1
Conductivity (σ)	0 (non-PEC), ∞(PEC)
E_0, H_0	1, 26.5×10^{-3}
Δn_{B}	3

respectively. The white squares represent the unidentified (U) SPs, where an appropriate IO could not be estimated from the MBRT algorithm. These SPs can also be interpreted as the MPCs scattered from chairs, tables, or small objects in the environment that were not modeled in the MBRT geometric map. As expected, the number of strong clusters decreased as the frequency increased, owing to larger path loss and scattering loss. The clusters were grouped well with only a few unidentified clusters. Moreover, the majority of clusters in terms of power contribution were SB clusters. Furthermore, there were some clusters that were mixtures of SB, DB, or TB clusters, owing to the lack of angular information at the Tx.

Fig. 9 illustrates the cluster tracking results at all three frequencies, and nine major clusters were identified as shown in Fig. 10, where a capital letter is used in the first letter to specify the cluster name and will be used for the rest of the paper. As expected, there were more powerful clusters at lower frequencies. Furthermore, most of the contributions among these clusters came from steel tubes, elevator, and metal studs, which have highly conducting surfaces.

B. FREQUENCY DEPENDENCY OF CLUSTER SI

With the assistance of PO, the clusters can be categorized into five groups as follows, where $SI_{3\ \mathrm{GHz}}$, $SI_{10\ \mathrm{GHz}}$, and $SI_{28\ \mathrm{GHz}}$ are the SI at 3, 10, and 28 GHz, respectively.

- Group 1: $SI_{3\ \mathrm{GHz}} \approx SI_{10\ \mathrm{GHz}} \approx SI_{28\ \mathrm{GHz}}$
- Group 2: $SI_{3\ \mathrm{GHz}} > SI_{10\ \mathrm{GHz}} > SI_{28\ \mathrm{GHz}}$
- Group 3: $SI_{28\ \mathrm{GHz}} > SI_{10\ \mathrm{GHz}} > SI_{3\ \mathrm{GHz}}$
- Group 4: $SI_{3\ \mathrm{GHz}} > SI_{28\ \mathrm{GHz}} > SI_{10\ \mathrm{GHz}}$
- Group 5: $SI_{10\ \mathrm{GHz}} > SI_{3\ \mathrm{GHz}} > SI_{28\ \mathrm{GHz}}$

Table 3 shows the mean and STD values of SI obtained from the measurement. All the snapshots of Pillar 1, Pillar 2, Tube+pillar, and Tubes 1 belong exclusively to group 1, and every snapshot of Brick belongs to group 2. The grouping and path trajectories of the cluster that belongs to more than one group are shown in Fig. 11. The detailed discussions of each group and their power contribution are provided in the subsequent sections. It should also be noted that the

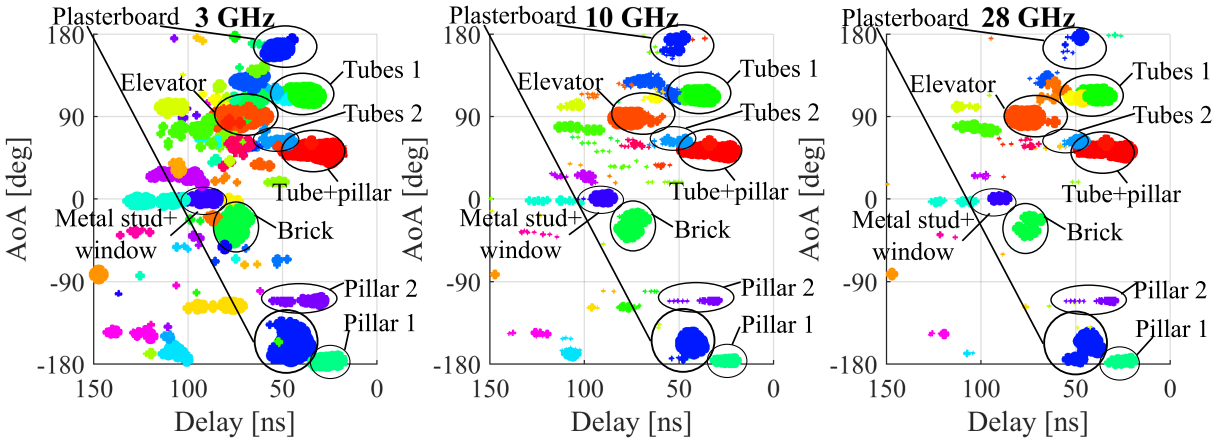

FIGURE 9. Cluster tracking results.

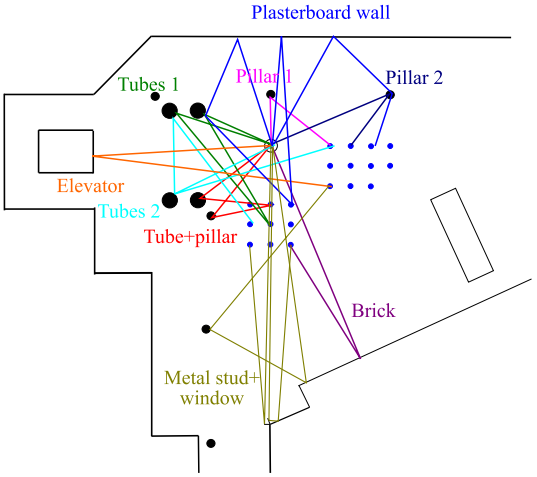

FIGURE 10. Major SB cluster trajectories.

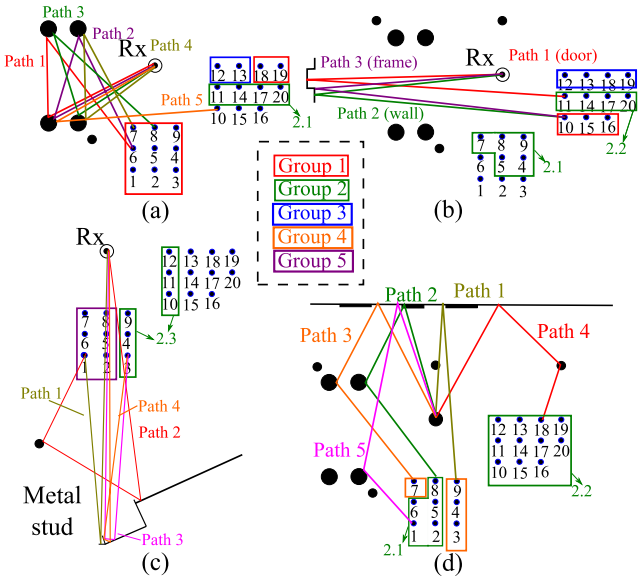

FIGURE 11. Grouping on the floor plan and path trajectories ((a) Tubes 2, (b) Elevator, (c) Metal stud+window, (d) Plasterboard wall).

LOS cluster is excluded from the analysis, as it is straightforward to model the frequency dependence.

1) GROUP 1

This group had no frequency dependence, mainly as a result of specular reflection on the cylindrical and smooth tube and pillar surfaces, where the reflection coefficients in these bands are similar [36], [37]. This includes all snapshots of Pillar 1, Pillar 2, Tube+pillar, and Tubes 1, and certain snapshots of Tubes 2 and Elevator. The STD was mostly less than 2 dB, owing to a small fading effect. Another mechanism in this group was the half Fresnel zone shadowing and scattering. Fig. 12 (a) shows the phase of Tubes 2, snapshot 18 (see path 5 of Fig. 11 (a)). The black straight lines represent the specular reflection trajectories, which were calculated from the Tx, Rx, and IO geometry. There was no frequency dependence, owing to two mechanisms in this figure: 1. Half Fresnel zone shadowing by a tube as the specular reflection trajectory was on its edge, 2. reflection from another tube behind the shadowing tube. The half Fresnel zone shadowing mechanism is similar to the half Fresnel zone scattering (see $d = 0$ of Fig. 3 (b)). Thus, it also had no frequency characteristics. In the case of Elevator, there were also no frequency characteristics, owing to the half Fresnel zone shadowing on both the Elevator door and wall.

2) GROUP 2

In this group, the SI decreased as the frequency increased because of three major mechanisms: 1. shadowing, 2. frame/rough surface scattering, and 3. diffraction/Fresnel zone plate effect. These mechanisms were divided into three subgroups, which will hereinafter be referred to as groups 2.1, 2.2, and 2.3.

The frequency characteristics of group 2.1 were due to the shadowing by tubes and pillars, which includes certain snapshots of Elevator, Tubes 2, and Plasterboard wall. Fig. 12 (b) shows the phase plot of Elevator at snapshot 8.

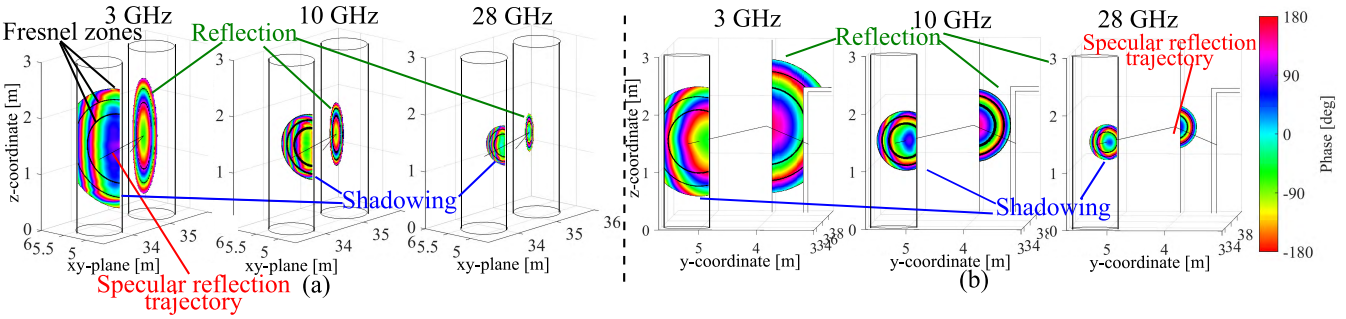

FIGURE 12. Phase plot on the surface of object in case of shadowing ((a) Tubes 2, snapshot 18, (b) Elevator, snapshot 8).

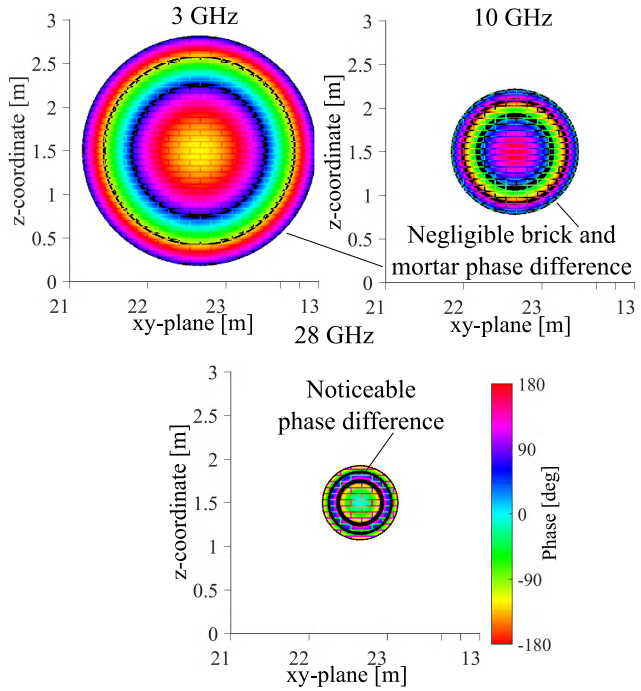

FIGURE 13. Phase plot on the surface of Brick wall, snapshot 18.

Because the specular reflection trajectory was inside the shadowing object, the shadowing effect at higher frequency was higher owing to the smaller Fresnel zones, which is similar to the effect of zone 5 from Fig. 3 (b).

Group 2.2 was frequency-dependent owing to scattering, which includes Brick and Plasterboard wall. Fig. 13 illustrates the phase plot of Brick at snapshot 18. Owing to the 2 mm gap between the brick and mortar, the SI decreased as the frequency increased, because the phase difference between them became more significant, which could also be interpreted as scattering loss. In contrast, the group 2 characteristics of Plasterboard wall were due to two mechanisms: 1. A larger degree of scattering from door frames and PEC studs behind plasterboard sheets due to larger Fresnel zones at 3 GHz, and 2. the multilayer structure of door and plasterboard caused the reflection coefficients to decrease as the frequency increased.

Group 2.3 had frequency characteristics as a result of diffraction from the Metal stud+window, which did not have a strong specular component, and the Fresnel zone plate effect from the Elevator. Fig. 14 (a) shows the phase plot of the Elevator at snapshot 11. The group 2 frequency dependence occurred because the second Fresnel zone of path 1 (see Fig. 11 (b)) at 3 GHz was shadowed by the outside wall of the Elevator, both on the right side and the top side, and the same effect also occurred at 10 GHz, but only on the left side. In contrast, reflection occurs at 28 GHz, as the Fresnel zones are smaller than the Elevator door.

Table 3 suggests that shadowing and diffraction effects created the large STD and SI differences among the different frequencies, whereas those differences for scattering and the Fresnel zone plate effect were not so large. These results imply that, although these effects were categorized into the same group, their sensitivities to the frequency characteristics were vastly different.

3) GROUP 3

The frequency dependence of this group occurred because of the Fresnel zone plate effect at 28 GHz and scattering/shadowing at other frequencies, which include the Elevator and Tubes 2. Fig. 14 (c) illustrates the phase plot of the Elevator at snapshot 12. The second Fresnel zone of path 1 at 28 GHz was shadowed on the right side, whereas scattering appeared at 10 and 3 GHz owing to the unevenness between the Elevator door and wall. In case of Tubes 2, the second Fresnel zone of path 5 at 28 GHz was shadowed by the tube, whereas the first Fresnel zone was partially shadowed at lower frequencies. Table 3 also indicates that these effects did not cause large STD and SI differences among the different frequencies, as only the Fresnel zone plate effect/scattering caused a frequency dependence.

4) GROUP 4

This group had the frequency dependence owing to two effects of the Plasterboard wall: First, the shadowing effect of path 1 was greater at higher frequencies as the specular reflection trajectory was inside the pillar. Therefore, the SI at 3 GHz was the highest. Second, the scattering effects from the PEC studs and door frame were greater at 28 GHz than at 10 GHz. Fig. 15 shows the phase plot of the second hop interaction of path 3 at 10 and 28 GHz. Because the stud size in terms of wavelength was larger at 28 GHz, its scattering influence increased. Such effects were also observed at

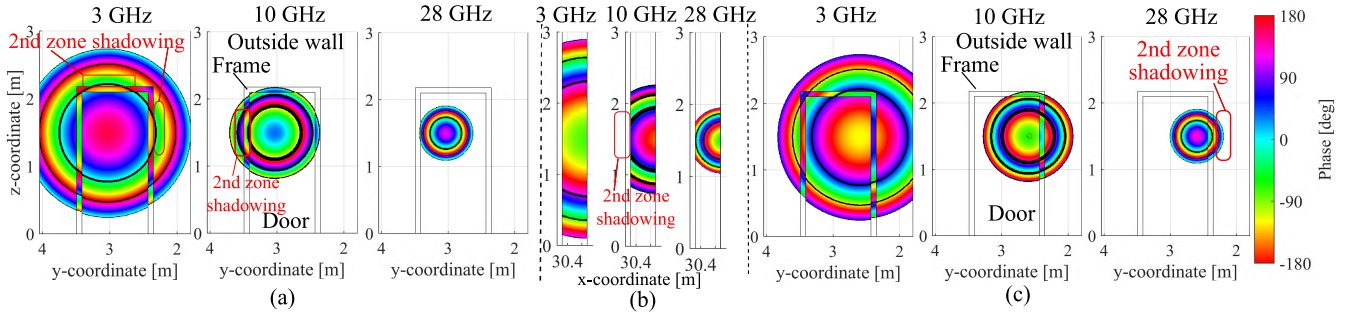

FIGURE 14. Phase plot on the surface of object in case of reflection with Fresnel zone plate effect ((a) Elevator, snapshot 11, (b) Metal stud, snapshot 6, (c) Elevator, snapshot 12).

TABLE 3. SI Mean and STD of clusters.

Group	Trend	Mechanism	Object	SI Mean (dB)			SI STD (dB)		
				3 GHz	10 GHz	28 GHz	3 GHz	10 GHz	28 GHz
1	$SI_{3\,\mathrm{GHz}} \approx SI_{10\,\mathrm{GHz}} \approx SI_{28\,\mathrm{GHz}}$	Reflection	Pillar 1	−18.6	−19.3	−20.2	1.1	0.6	1.8
			Pillar 2	−20.4	−21.7	−21.8	1.8	0.7	1.2
			Tube+pillar	−9.9	−10.6	−10.4	1.1	1	0.8
			Tubes 1	−9.7	−9.2	−9.8	1.7	1.9	0.9
		Reflection+ Shadowing	Elevator	−2.1	−2.2	−1.1	0.5	1.2	1.8
			Tubes 2	−16.6	−16.8	−16.9	0	0	0
	$SI_{3\,\mathrm{GHz}} \approx SI_{10\,\mathrm{GHz}}$	Reflection	Tubes 2	−18.6	−18.4	NA	2.8	1.2	NA
2.1	$SI_{3\,\mathrm{GHz}} > SI_{10\,\mathrm{GHz}} > SI_{28\,\mathrm{GHz}}$	Reflection+ Shadowing	Elevator	−5.7	−12.9	−13.7	1	3.2	2.5
	$SI_{3\,\mathrm{GHz}} > SI_{10\,\mathrm{GHz}}$		Elevator	−11.1	−19.1	NA	4.5	1.5	NA
			Tubes 2	−19.8	−24.1	NA	1.5	1.9	NA
			Plasterboard wall	−8.6	−13.5	NA	1.6	2.8	NA
2.2	$SI_{3\,\mathrm{GHz}} \approx SI_{10\,\mathrm{GHz}} > SI_{28\,\mathrm{GHz}}$	Frame/ rough surface scattering	Brick wall	−5.4	−6.8	−10.9	1.7	1.3	2.6
	$SI_{3\,\mathrm{GHz}} > SI_{10\,\mathrm{GHz}} > SI_{28\,\mathrm{GHz}}$		Plasterboard wall	−4.4	−7.3	−9.7	1.1	1.6	2.5
2.3	$SI_{3\,\mathrm{GHz}} > SI_{10\,\mathrm{GHz}} \approx SI_{28\,\mathrm{GHz}}$	Diffraction/ 3 GHz Fresnel zone plate effect/ scattering	Elevator	5.3	0.7	0.9	0.4	1	0.9
	$SI_{3\,\mathrm{GHz}} > SI_{10\,\mathrm{GHz}}$		Metal stud+ window	−9.4	−14.3	NA	3	3.2	NA
3	$SI_{28\,\mathrm{GHz}} > SI_{10\,\mathrm{GHz}} > SI_{3\,\mathrm{GHz}}$	Fresnel zone plate effect at 28 GHz	Tubes 2	−14.2	−12.4	−10.5	1.1	2	0.6
	$SI_{28\,\mathrm{GHz}} > SI_{10\,\mathrm{GHz}} \approx SI_{3\,\mathrm{GHz}}$		Elevator	−2.1	−2.1	1.1	0.5	0.1	1.1
4	$SI_{3\,\mathrm{GHz}} > SI_{28\,\mathrm{GHz}} > SI_{10\,\mathrm{GHz}}$	Shadowing+scattering	Plasterboard wall	−8.9	−13.1	−10.3	1.2	2.3	1.9
5	$SI_{10\,\mathrm{GHz}} > SI_{3\,\mathrm{GHz}} > SI_{28\,\mathrm{GHz}}$	10 GHz Fresnel zone plate effect/ scattering	Metal stud+ window	−6.5	−3.3	−8.8	2	1.2	1.6

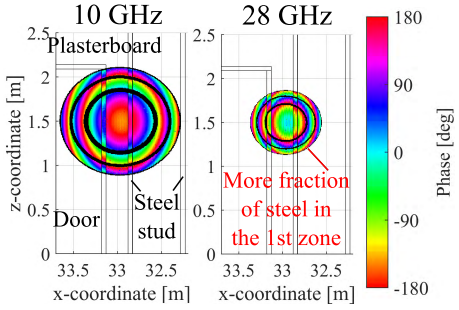

FIGURE 15. Phase plot on the surface of Plasterboard wall, snapshot 3, path 3.

paths 2 and 5. Therefore, these collectively lead to a higher SI at 28 GHz compared to that at 10 GHz. Table 3 also implies that the STD and SI differences among the different frequencies were not so large, as the shadowing and scattering effects were similar across the snapshots.

5) GROUP 5

This group was frequency-dependent because of the Fresnel zone plate effect and scattering at other frequencies, which includes only Metal stud+window. Fig. 14 (b) shows the phase plot of this cluster. It can be observed that the second Fresnel zone at 10 GHz disappeared at the edge of the stud, whereas the scattering effect occurred at other frequencies. Table 3 also indicates that the STD and SI differences among the different frequencies were not so large, as the Fresnel zone plate effect and scattering were the mechanisms that produced the frequency characteristics.

6) GROUP CONTRIBUTION TO THE CHANNEL

To check the significance of each cluster, its power in relation to the total power was calculated in each snapshot by calculating the ratio of the cluster power to the total channel power, excluding the LOS clusters to mimic the obstructed LOS (OLOS) channel. Fig. 16 (a) and (b) show the power percentage contributions for each snapshot and all the snapshots.

Fig. 16 (a) revealed that these nine clusters from all five groups contributed approximately 60–80% for the 3 GHz case, and 80–90% for the 10 and 28 GHz cases. The contribution at 3 GHz was lower, because there were more scattering components. From snapshots 1–10, where reflection and

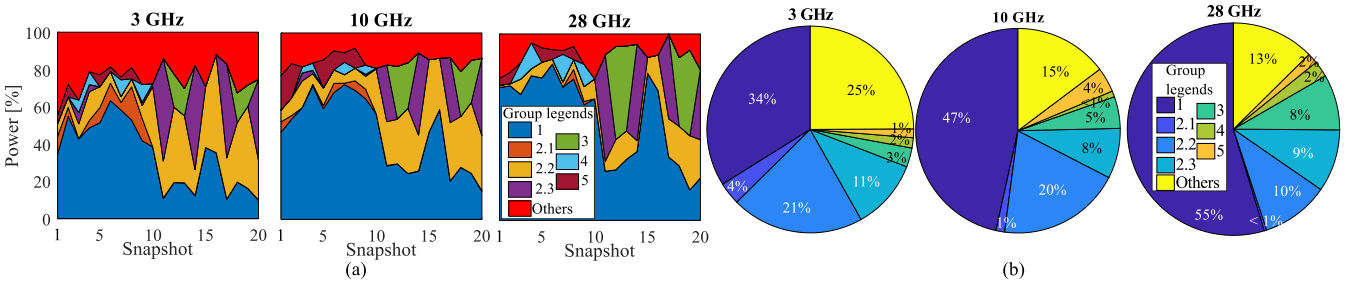

FIGURE 16. Power contribution of each group ((a) Each snapshot, (b) All snapshots).

scattering from Elevator and Plasterboard wall were shadowed by tubes and pillars, group 1 became dominant. Most contributions of group 1 came from reflection and half Fresnel zone scattering from tubes and Elevator, as they have large and smooth conducting surfaces. Group 4 from Plasterboard wall scattering and group 5 from the Fresnel zone plate effect on Metal stud+window also had some contributions at these snapshots, but not as significant as those of group 1. From snapshots 11–20, owing to the Fresnel zone plate effect from Elevator and Tubes 2, and scattering from Plasterboard wall, the contribution from groups 2–3 became prominent. One exception during these snapshots is at snapshots 15 and 16, where the reflection from Elevator with half Fresnel zone shadowing contributed greatly to group 1.

Fig. 16 (b) implied that groups 1–3 dictated the channel, where the power contribution of groups 1 and 3 increased as the frequency increased. On the contrary, the contribution of group 2 reduced as the frequency increased. This implies that the overall channel tended to become more directive when the frequency increased, owing to the higher significance of reflection and lower influence of scattering/diffraction/shadowing, which is also consistent with previously published works [5], [13], [14], [23]. Therefore, these mechanisms that caused the frequency characteristics were not negligible and must be considered.

VI. CONCLUSION

In summary, a frequency dependency analysis of geometry-based clusters in an indoor environment at SHF bands was carried out and discussed. The MPC parameters were estimated by using the SAGE algorithm. After that, SIMO-based SPKPM was applied to estimate the clusters. Finally, the frequency dependency analysis and physical interpretation of the cluster SI were carried out with the assistance of PO.

Owing to the large room size, the LOS and SB clusters contributed to the majority of the total channel power and nine major clusters were detected. These nine clusters accounted for 60–80% of the total channel power at 3 GHz and 80–90% of the total cluster power for 10 and 28 GHz, owing to fewer scattering components. The frequency dependency analysis illustrated that the clusters could be classified into five groups, but groups 1–3 dominated the channel. Group 1, which was frequency-independent owing to specular reflection and half Fresnel zone shadowing/scattering from tubes, pillars, and the elevator, contributed the most. The STD was small owing to a small fading effect and the power contribution of this group increased as the frequency increased. On the contrary, the frequency dependence of group 2 was due to shadowing, scattering, diffraction, and the Fresnel zone plate effect, and the power contribution of this group decreased as the frequency increased. The frequency dependencies of shadowing and diffraction were also higher than those of scattering and the Fresnel zone plate effect. Similar to group 1, the power contribution of group 3 increased as the frequency increased, owing to the Fresnel zone plate effect at 28 GHz. In contrast, groups 4–5 showed varying small contributions, especially at snapshots 1–9. This suggested that the overall channel had the tendency to become more directive as the frequency increased, owing to stronger specular reflection compared with shadowing, scattering, and diffraction. However, the channel still showed strong frequency dependence because the shadowing, scattering, diffraction, and Fresnel zone plate effects were not negligible, especially at lower frequencies. Thus, special care is needed to characterize the channel at several bands. In our future work, the same analysis approach will be applied to another type of environment.

ACKNOWLEDGMENT

The authors would like to thank Kim Olesen and Kristian Bank for the channel sounding setup.

REFERENCES

[1] K. Sakaguchi, E. M. Mohamed, H. Kusano, M. Mizukami, S. Miyamoto, R. E. Rezagah, K. Takinami, K. Takahashi, N. Shirakata, H. Peng, T. Yamamoto, and S. Namba, "Millimeter-wave wireless LAN and its extension toward 5G heterogeneous networks," *IEICE Trans. Commun.*, vols. E98-B, no. 10, pp. 1932–1948, Jul. 2015.

[2] T. S. Rappaport, S. Sun, R. Mayzus, H. Zhao, Y. Azar, K. Wang, G. N. Wong, J. K. Schulz, M. Samimi, and F. Gutierrez, "Millimeter wave mobile communications for 5G cellular: It will work!" *IEEE Access*, vol. 1, pp. 335–349, 2013.

[3] *Final Acts WRC-15*, Int. Telecommun. Union, Geneva, Switzerland, 2015.

[4] K. Haneda, "Channel models and beamforming at millimeter-wave frequency bands," *IEICE Trans. Commun.*, vol. E98-B, no. 5, pp. 755–772, May 2015.

[5] W. Fan, I. Carton, J. Ø. Nielsen, K. Olesen, and G. F. Pedersen, "Measured wideband characteristics of indoor channels at centimetric and millimetric bands," *EURASIP J. Wireless Commun. Netw.*, vol. 2016, no. 1, p. 58, Feb. 2016.

[6] W. Fan, I. Carton, and G. F. Pedersen, "Comparative study of centimetric and millimetric propagation channels in indoor environments," in *Proc. 10th Eur. Conf. Antennas Propag. (EuCAP)*, Apr. 2016, pp. 1–5.

[7] J. Hejselbaek, W. Fan, and G. F. Pedersen, "Ultrawideband VNA based channel sounding system for centimetre and millimetre wave bands," in *Proc. IEEE 27th Annu. Int. Symp. Pers., Indoor, Mobile Radio Commun. (PIMRC)*, Sep. 2016, pp. 1–6.
[8] J. Medbo, N. Seifi, and H. Asplund, "Frequency dependency of measured highly resolved directional propagation channel characteristics," in *Proc. 22th Eur. Wireless Conf., Eur. Wireless*, May 2016, pp. 1–6.
[9] G. R. Maccartney, T. S. Rappaport, S. Sun, and S. Deng, "Indoor office wideband millimeter-wave propagation measurements and channel models at 28 and 73 GHz for ultra-dense 5G wireless networks," *IEEE Access*, vol. 3, pp. 2388–2424, 2015.
[10] S. Deng, M. K. Samimi, and T. S. Rappaport, "28 GHz and 73 GHz millimeter-wave indoor propagation measurements and path loss models," in *Proc. IEEE Int. Conf. Commun. Workshop (ICCW)*, Jun. 2015, pp. 1244–1250.
[11] K. Haneda, J. Järveläinen, A. Karttunen, M. Kyrö, and J. Putkonen, "Indoor short-range radio propagation measurements at 60 and 70 GHz," in *Proc. 8th Eur. Conf. Antennas Propag.*, Apr. 2014, pp. 634–638.
[12] K. Haneda, J. Järveläinen, A. Karttunen, M. Kyrö, and J. Putkonen, "A statistical spatio-temporal radio channel model for large indoor environments at 60 and 70 GHz," *IEEE Trans. Antennas Propag.*, vol. 63, no. 6, pp. 2694–2704, Jun. 2015.
[13] J. Vehmas, J. Järveläinen, S. Le Hong Nguyen, R. Naderpour, and K. Haneda, "Millimeter-wave channel characterization at Helsinki airport in the 15, 28, and 60 GHz bands," in *Proc. IEEE 84th Veh. Technol. Conf. (VTC-Fall)*, Sep. 2016, pp. 1–5.
[14] U. T. Virk, S. L. H. Nguyen, and K. Haneda, "Multi-frequency power angular spectrum comparison for an indoor environment," in *Proc. 11th Eur. Conf. Antennas Propag. (EUCAP)*, Mar. 2017, pp. 3389–3393.
[15] M. Peter and W. Keusgen, "Analysis and comparison of indoor wideband radio channels at 5 and 60 GHz," in *Proc. 3rd Eur. Conf. Antennas Propag.*, Mar. 2009, pp. 3830–3834.
[16] M. Sasaki, M. Inomata, W. Yamada, N. Kita, T. Onizawa, and M. Nakatsugawa, "Path loss characteristics at multiple frequency bands from 0.8 to 37 GHz in indoor office," in *Proc. 10th Eur. Conf. Antennas Propag. (EuCAP)*, Apr. 2016, pp. 1–4.
[17] J. Huang, C.-X. Wang, R. Feng, J. Sun, W. Zhang, and Y. Yang, "Multi-frequency mmWave massive MIMO channel measurements and characterization for 5G wireless communication systems," *IEEE J. Sel. Areas Commun.*, vol. 35, no. 7, pp. 1591–1605, Jul. 2017.
[18] F. Huang, L. Tian, Y. Zheng, and J. Zhang, "Propagation characteristics of indoor radio channel from 3.5 GHz to 28 GHz," in *Proc. IEEE 84th Veh. Technol. Conf. (VTC-Fall)*, Sep. 2016, pp. 1–5.
[19] J.-Z. Li, B. Ai, R.-S. He, Q. Wang, M. Yang, B. Zhang, K. Guan, D.-P. He, Z.-D. Zhong, T. Zhou, and N. Li, "Indoor massive multiple-input multiple-output channel characterization and performance evaluation," *Frontiers Inf. Technol. Electron. Eng.*, vol. 18, no. 6, pp. 773–787, Jun. 2017.
[20] J. Lee, J. Liang, M.-D. Kim, J.-J. Park, B. Park, and H. K. Chung, "Measurement-based propagation channel characteristics for millimeter-wave 5G Giga communication systems," *ETRI J.*, vol. 38, no. 6, pp. 1031–1041, Dec. 2016.
[21] J.-J. Park, J. Liang, J. Lee, H.-K. Kwon, M.-D. Kim, and B. Park, "Millimeter-wave channel model parameters for urban microcellular environment based on 28 and 38 GHz measurements," in *Proc. IEEE 27th Annu. Int. Symp. Pers., Indoor, Mobile Radio Commun. (PIMRC)*, Sep. 2016, pp. 1–5.
[22] A. Bamba, F. Mani, and R. D'Errico, "A comparison of indoor channel properties in V and E bands," in *Proc. 11th Eur. Conf. Antennas Propag. (EUCAP)*, Mar. 2017, pp. 3361–3365.
[23] P. Hanpinitsak, K. Saito, W. Fan, J.-I. Takada, and G. F. Pedersen, "Frequency characteristics of path loss and delay-angular profile of propagation channels in an indoor room environment in SHF bands," in *Proc. IEICE Mobile Commun. Workshop*, Mar. 2017, pp. 153–158.
[24] G. Zhang, P. Hanpinitsak, X. Cai, W. Fan, K. Saito, J.-I. Takada, and G. F. Pedersen, "Millimeter-wave channel characterization in large hall scenario at the 10 and 28 GHz bands," in *Proc. Eur. Conf. Antennas Propag.*, Mar. 2019, pp. 1–5.
[25] L. Liu, C. Oestges, J. Poutanen, K. Haneda, P. Vainikainen, F. Quitin, F. Tufvesson, and P. D. Doncker, "The COST 2100 MIMO channel model," *IEEE Wireless Commun.*, vol. 19, no. 6, pp. 92–99, Dec. 2012.
[26] R. J. Weiler, M. Peter, W. Keusgen, A. Maltsev, I. Karls, A. Pudeyev, I. Bolotin, I. Siaud, and A.-M. Ulmer-Moll, "Quasi-deterministic millimeter-wave channel models in MiWEBA," *EURASIP J. Wireless Commun. Netw.*, vol. 2016, no. 1, p. 84, Mar. 2016.
[27] N. Czink, P. Cera, J. Salo, E. Bonek, J.-P. Nuutinen, and J. Ylitalo, "A framework for automatic clustering of parametric MIMO channel data including path powers," in *Proc. IEEE Veh. Technol. Conf.*, Sep. 2006, pp. 1–5.
[28] *Technical Specification Group Services and System Aspects (Release 15) Version 1.0.0*, document TR 21.915, 3GPP, Mar. 2019.
[29] M. Peter, "Measurement results and final mmMAGIC channel models," mm-Wave based Mobile Radio Access Netw. 5G Integr. Commun., Tech. Rep. H2020-ICT-671650-mmMAGIC/D2.2, May 2017.
[30] P. Hanpinitsak, K. Saito, J.-I. Takada, M. Kim, and L. Materum, "Multi-path clustering and cluster tracking for geometry-based stochastic channel modeling," *IEEE Trans. Antennas Propag.*, vol. 65, no. 11, pp. 6015–6028, Nov. 2017.
[31] M. Zhu, "Geometry-based radio channel characterization and modeling: Parameterization, implementation and validation," Ph.D. dissertation, Dept. Elect. Inf. Technol., Lund Univ., Lund, Sweden, Aug. 2014.
[32] B. H. Fleury, M. Tschudin, R. Heddergott, D. Dahlhaus, and K. I. Pedersen, "Channel parameter estimation in mobile radio environments using the SAGE algorithm," *IEEE J. Sel. Areas Commun.*, vol. 17, no. 3, pp. 434–450, Mar. 1999.
[33] P. Hanpinitsak, K. Saito, J. Takada, M. Kim, and L. Materum, "Clustering method based on scatterer locations for indoor dynamic MIMO channel," in *Proc. 10th Eur. Conf. Antennas Propag. (EuCAP)*, Apr. 2016, pp. 1–4.
[34] E. Yamashita, *Analysis Methods for Electromagnetic Wave Problems*. Norwood, MA, USA: Artech House, 1990.
[35] K. Wangchuk, K. Umeki, T. Iwata, P. Hanpinitsak, M. Kim, K. Saito, and J.-I. Takada, "Double directional millimeter wave propagation channel measurement and polarimetric cluster properties in outdoor urban pico-cell environment," *IEICE Trans. Commun.*, vols. E100-B, no. 7, pp. 1133–1144, Jul. 2017.
[36] D. Ferreira, I. Cuiñas, R. F. S. Caldeirinha, and T. R. Fernandes, "A review on the electromagnetic characterisation of building materials at micro- and millimetre wave frequencies," in *Proc. 8th Eur. Conf. Antennas Propag.*, Apr. 2014, pp. 145–149.
[37] G. Tesserault, N. Malhouroux, and P. Pajusco, "Determination of material characteristics for optimizing WLAN radio," in *Proc. Eur. Conf. Wireless Technol.*, Oct. 2007, pp. 225–228.
[38] L. Materum, J.-I. Takada, I. Ida, and Y. Oishi, "Mobile station spatio-temporal multipath clustering of an estimated wideband MIMO double-directional channel of a small urban 4.5 GHz macrocell," *EURASIP J. Wireless Commun. Netw.*, vol. 2009, no. 1, Dec. 2009, Art. no. 804021.
[39] N. Lertsirisopon, G. S. Ching, M. Ghoraishi, J.-I. Takada, I. Ida, and Y. Oishi, "Investigation of non-specular scattering by comparing directional channel characteristics from microcell measurement and simulation," *IET Microw., Antennas Propag.*, vol. 2, no. 8, pp. 913–921, Dec. 2008.
[40] J. Poutanen, K. Haneda, J. Salmi, V.-M. Kolmonen, A. Richter, P. Almers, and P. Vainikainen, "Development of measurement-based ray tracer for multi-link double directional propagation parameters," in *Proc. 3rd Eur. Conf. Antennas Propag.*, Mar. 2009, pp. 2622–2626.
[41] T. Miyake, "Numerical simulation of scattering from random rough surface by using physical optics," M.S. thesis, Tokyo Inst. Technol., Tokyo, Japan, Feb. 2018.
[42] C. A. Balanis, *Advanced Engineering Electromagnetics*. Hoboken, NJ, USA: Wiley, 2012.
[43] A. Ludwig, "Computation of radiation patterns involving numerical double integration," *IEEE Trans. Antennas Propag.*, vol. 16, no. 6, pp. 767–769, Nov. 1968.
[44] M. L. X. D. Santos and N. R. Rabelo, "On the Ludwig integration algorithm for triangular subregions," *Proc. IEEE*, vol. 74, no. 10, pp. 1455–1456, Oct. 1986.
[45] T. Kohama and M. Ando, "Localization of radiation integrals using the fresnel zone numbers," *IEICE Trans. Electron.*, vol. E95.C, no. 5, pp. 928–935, 2012.
[46] H. D. Hristov and M. H. A. J. Herben, "Millimeter-wave fresnel-zone plate lens and antenna," *IEEE Trans. Microw. Theory Techn.*, vol. 43, no. 12, pp. 2779–2785, Dec. 1995.
[47] J. C. Schelleng, C. R. Burrows, and E. B. Ferrell, "Ultra-short-wave propagation," *Proc. Inst. Radio Eng.*, vol. 21, no. 3, pp. 427–463, Mar. 1933.
[48] S. S. Zhekov, A. Tatomirescu, and G. F. Pedersen, "Modified biconical antenna for ultrawideband applications," in *Proc. 10th Eur. Conf. Antennas Propag. (EuCAP)*, Apr. 2016, pp. 1–5.

[49] G. Zhang, k. Saito, W. Fan, X. Cai, P. Hanpinitsak, J.-I. Takada, and G. F. Pedersen, "Experimental characterization of millimeter-wave indoor propagation channels at 28 GHz," *IEEE Access*, vol. 6, pp. 76516–76526, 2018.

[50] Knauf. *Installation: A Detailed Insight Into how to Handle and Mount Plasterboard on a Stud Frame*. Accessed: Nov. 26, 2018. [Online]. Available: https://mdbapi.knauf.com/v1/pdf_download.php?action=download&a=732006&c=a4ef762ba12191cc78c9a98ee1d17da4&p=g

[51] *Vd 9 Massiv Innerdörr (in Swedish)*. Accessed: Nov. 26, 2018. [Online]. Available: http://sscgroup.se/produkt/vd-9-massiv-innerdorr/

[52] H. V. Pham, M. Kim, and J.-I. Takada, "Cluster-based indoor radio channel characterization at 11 GHz," IEICE, Tokyo, Japan, Tech. Rep. 487, AP2013-200, Mar. 2014.

[53] Y. Ji, W. Fan, and G. F. Pedersen, "Channel estimation using spherical-wave model for indoor LoS and obstructed LoS scenarios," in *Proc. 11th Eur. Conf. Antennas Propag. (EUCAP)*, Mar. 2017, pp. 2459–2462.

[54] K. Haneda, J.-I. Takada, and T. Kobayashi, "A parametric UWB propagation channel estimation and its performance validation in an anechoic chamber," *IEEE Trans. Microw. Theory Techn.*, vol. 54, no. 4, pp. 1802–1811, Jun. 2006.

PANAWIT HANPINITSAK (S'17) was born in 1991. He received the B.E. degree (Hons.) in electronics and communications engineering from the Sirindhorn International Institute of Technology, Thammasat University, Pathumthani, Thailand, in 2013, and the M.E. degree in international development engineering, majoring in electrical/electronic engineering from the Tokyo Institute of Technology, Japan, in 2016, where he is currently pursuing the D.E. degree. His research interests include channel parameter estimation and beamforming algorithms, and radio propagation channel modeling at millimeter waves. He was a Guest Ph.D. Researcher with Aalborg University, Denmark, and Ilmenau University of Technology, Germany, in 2016 and 2018, respectively. He received the Best Student Presentation Award at the IEICE Short Range Wireless (SRW) conference, in 2017. He is a student member of the IEICE.

KENTARO SAITO (M'17) was born in Kanagawa, Japan, in 1977. He received the B.S. and Ph.D. degrees from the University of Tokyo, Japan, in 2002 and 2008, respectively.

He joined NTT DOCOMO, Kanagawa, Japan, in 2002. Since 2002, he has been engaged in the research and development of mobile communication systems and radio propagation. He joined the Tokyo Institute of Technology, Japan, in 2015. Since 2015, he has been engaged in the research on radio propagation for mobile communication systems.

Dr. Saito is a member of the IEICE.

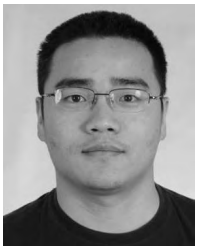

WEI FAN received the B.E. degree from the Harbin Institute of Technology, China, in 2009, the master's double degree (Hons.) from Politecnico di Torino, Italy, and the Grenoble Institute of Technology, France, in 2011, and the Ph.D. degree from Aalborg University, Denmark, in 2014. In 2011, he was with Intel Mobile Communications, Denmark, as a Research Intern. He held a three-month internship at Anite Telecoms Oy, Finland, in 2014. He is currently an Associate Professor at the Antennas, Propagation, and Millimeter-wave Systems (APMS) Section, Aalborg University. His main research interests include over-the-air testing of multiple antenna systems, radio channel sounding, modeling, and emulation.

JOHANNES HEJSELBÆK (S'15–M'18) received the B.Sc. in electronic engineering, M.Sc. in wireless communication systems, and Ph.D. degree in wireless communication systems from the Section for Antennas, Propagation, and Millimeter-wave Systems (APMS), Department of Electronic Systems, Aalborg University, in 2013, 2015, and 2018, respectively. The focus for his Ph.D. was on channel characterization and electromagnetic modeling for the fifth-generation communication systems. During the B.Sc. studies, he visited Huawei, China, and during the M.Sc., he was a Research Intern at Intel Mobile Communication, Denmark. His Ph.D. Fellowship was conducted within the VIRTUOSO project supported by the Innovation Fund Denmark, Telenor, Keysight, and Intel Mobile Communications. He was a Guest Ph.D. Researcher at the Tokyo Institute of Technology, Japan, in 2018. He is currently with Nokia Bell Labs, Denmark.

JUN-ICHI TAKADA (S'89–M'93–SM'11) received the B.E., M.E., and D.E. degrees in electrical and electronic engineering from the Tokyo Institute of Technology, Tokyo, Japan, in 1987, 1989, and 1992, respectively.

He was a Research Associate with Chiba University, Chiba, Japan, from 1992 to 1994, and an Associate Professor with the Tokyo Institute of Technology, from 1994 to 2006. He has been a Professor with the Tokyo Institute of Technology, since 2006. He was also a Researcher with the National Institute of Information and Communications Technology, Kanagawa, Japan, from 2003 to 2007. His research interests include radio-wave propagation and channel modeling for mobile and short-range wireless systems, regulatory issues of spectrum sharing, and ICT applications for international development.

Prof. Takada is a fellow of the IEICE, Japan.

GERT FRØLUND PEDERSEN was born in 1965. He received the B.Sc. E.E. degree (Hons.) in electrical engineering from the College of Technology in Dublin, Ireland, in 1991, and the M.Sc. E.E. and Ph.D. degrees from Aalborg University, in 1993 and 2003, respectively. He has been with Aalborg University, since 1993, where he is currently a Full Professor, heading the Antenna, Propagation, and Networking Laboratory with 36 researchers. He is also the Head of the Doctoral School on Wireless Communication, with approximately 100 Ph.D. students enrolled. His research has focused on radio communication for mobile terminals, especially small antennas, diversity systems, propagation, and biological effects. He has published more than 175 peer-reviewed papers and holds 28 patents. He was a Consultant for the development of more than 100 antennas for mobile terminals, including the first internal antenna for mobile phones, in 1994, with lowest SAR, first internal triple-band antenna, in 1998, with low SAR and high TRP and TIS, and recently various multi-antenna systems rated as the most efficient on the market. He has worked most of the time with joint university–industry projects and has received more than $12 M in direct research funding. Most recently, he is the project leader of the SAFE project, with a total budget of $8 M, investigating tunable front-ends, including tunable antennas for future multiband mobile phones. He was one of the pioneers in establishing over-the-air (OTA) measurement systems, the measurement techniques of which are now well-established for mobile terminals with single antennas. He also chaired various COST groups (swg2.2 of COST 259, 273, 2100, and now ICT1004) with liaison to 3GPP for OTA test of MIMO terminals. Currently, he is deeply involved in MIMO OTA measurements.